


## Missing-rung problem in vibrational ladder climbing

Takahiro Horiba , Soichi Shirai, and Hirotohi Hirai\*

Toyota Central Research and Development Labs., Inc., 41-1, Yokomichi, Nagakute, Aichi 480-1192, Japan



(Received 1 September 2021; revised 21 December 2021; accepted 6 January 2022; published 26 January 2022)

Vibrational ladder climbing (VLC), which is a cascade excitation process of molecular vibrational levels under chirped laser pulses, is one of the promising methods to realize molecular bond breaking, but there have been few experimental reports on bond breaking by VLC. In this study we observed vanishing of the transition dipole moment, interrupting VLC in general molecular systems. This phenomenon, that adjacent transition is forbidden at a certain vibrational level, was found to be explained by the parities of the dipole function and the vibrational wave functions. In order to preserve VLC, we proposed a method to use an additional chirped pulse that realizes “double-stepping” transitions at levels where adjacent transitions are forbidden. To show the effectiveness of our method, we conducted wave-packet dynamics simulations for LiH dissociations with chirped pulses. The results indicate that the efficiency of LiH dissociation is significantly improved by our method compared to conventional VLC methods with a single pulse. We also revealed the quantum interference effect behind the excitation process of VLC and found that the relative phase between the main pulse and the additional pulse has a significant effect on the dissociation probabilities of molecules.

DOI: [10.1103/PhysRevA.105.013117](https://doi.org/10.1103/PhysRevA.105.013117)

### I. INTRODUCTION

Controlling molecular reactions as desired is one of the ultimate goals of chemical physics. Compared to conventional macroscopic reaction control methods using temperature and pressure, proposed methods that directly control the quantum state of molecules using the electric field of a laser are expected to achieve dramatically improved efficiency and selectivity of reactions [1–3]. Such techniques, first proposed by Brumer and Shapiro in the 1980s [1], are called “coherent control,” and with the advent of femtosecond pulsed lasers and the development of laser shaping technology have been the subject of numerous studies and continue to attract considerable attention [4–6]. A promising coherent control method is vibrational ladder climbing (VLC) [7], which employs a cascade excitation process in molecular vibrational levels under chirped infrared laser pulses with time-dependent frequencies corresponding to the vibrational excitation energy levels. VLC can focus an input laser pulse energy on a specific molecular bond. Thereby, it is expected to realize highly efficient bond-selective photodissociation [8]. VLC has been studied intensively both experimentally and theoretically. Experimentally, the vibrational excitation by VLC in diatomic molecules (NO [9], HF [10]) and amino acids [11] has been reported. Recently, Morichika *et al.* succeeded in breaking molecular bonds in transition-metal carbonyl  $\text{WCO}_6$  with a chirped infrared pulse enhanced by surface plasmon resonance [8]. Unfortunately, there are few experimental reports of successful bond breaking by VLC, which remains a challenge. In early theoretical works, Liu *et al.* and Duan *et al.* studied the classical motion of driven Morse oscillators [12–14]. They analyzed the excitation and dissociation dynamics of diatomic

molecules under a chirped electric field using the action-angle variable, and found the condition for efficient excitation [12,13]. Regarding the quantum aspects, a pioneering work by Marcus *et al.* [15] focused on quantum and classical excitation processes, specifically quantum ladder climbing and classical autoresonance, and proposed parameters to characterize the quantum and classical phenomena [15,16]. Based on the characterization parameters, quantum and classical comparisons were made in various systems [17–20] such as plasma systems [21] and superconducting circuits [22]. The excitation condition proposed by Yuan *et al.* and the characterization parameters proposed by Marcus *et al.* depend on the physical properties of the system such as the potential energy surface (PES) and the dipole function. Thereby, these properties determine the characteristic of VLC. However, most of the theoretical treatments were based on simple model functions of these properties such as Morse potentials and linear dipole moments [12,15,23–25].

In this study, we performed wave-packet dynamics simulations of VLC based on the PES and the dipole moment computed by a highly accurate *ab initio* quantum chemistry method. The results of the simulations revealed a problem that has not previously been recognized in VLC: VLC is interrupted by the existence of a level with a nearly zero adjacent transition dipole moment (TDM), i.e., vanishing of the TDM. We call this problem the missing-rung problem (MRP) as it is like a rung missing in the middle of a ladder.

### II. MISSING-RUNG PROBLEM

The lower panels of Figs. 1(b) and 1(c) show the absolute values of TDMs for the diatomic molecules LiH and HF, respectively. It can be seen that the TDMs of the 16th level of LiH and the 12th level of HF have nearly zero values, which indicate “missing rungs” in the vibrational levels. To

\*hirotoshih@mosk.tytlabs.co.jp

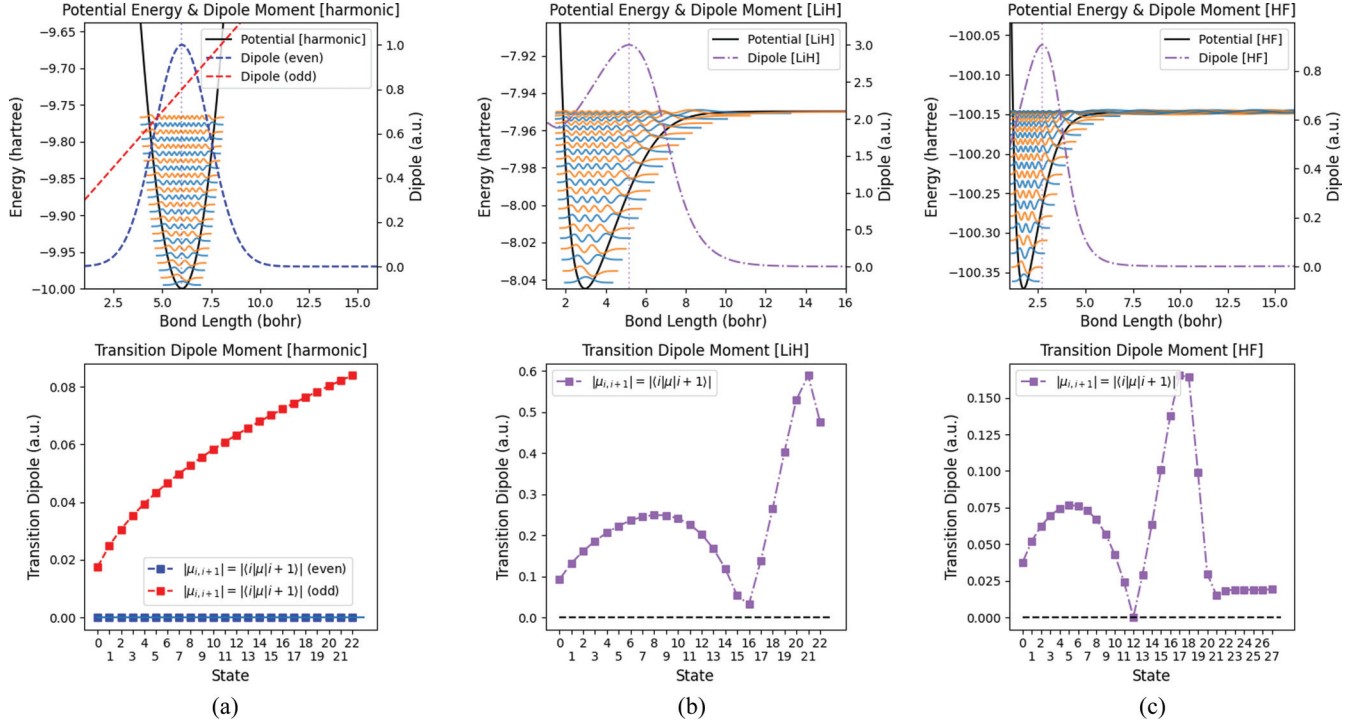


FIG. 1. Top: PESs and dipole moments for (a) the harmonic model, (b) the LiH molecule, and (c) the HF molecule. For the harmonic model, the model dipole moments are shown. The orange and light blue lines show the vibrational wave functions. Bottom: Absolute values of the corresponding TDMs.

understand the cause of the MRP, we start by considering a harmonic oscillator. The vibrational wave functions of the harmonic potential  $|\phi_i\rangle$  are described by Hermite polynomials, and their parities are different between adjacent levels, as described in Fig. 1(a). Assuming an odd function for the dipole moment, the TDM between adjacent levels  $\mu_{i,i+1} = \langle \phi_i | \mu | \phi_{i+1} \rangle$  becomes an integral of an even function, which yields a nonzero value (i.e., an allowed transition). The well-known infrared selection rule  $\Delta v = \pm 1$  corresponds to this result [26]. On the other hand, if we assume an even function for the dipole moment, the adjacent TDM  $\mu_{i,i+1}$  becomes an integral of an odd function, which yields zero (i.e., a forbidden transition), as shown in the lower panel of Fig. 1(a).

Based on the above discussions, we consider two realistic molecular systems, LiH and HF, where the shapes of the vibrational wave functions of molecules are similar to those of a harmonic potential except for a distortion due to the anharmonicity of the PESs, as shown in Figs. 1(b) and 1(c). Therefore, the nature of the parity of the wave functions is approximately conserved, whereas the parity of molecular dipole moments is not as simple as in the above discussion for the harmonic potential. In the following discussion on the parity, the coordinate origin is taken to be the center of the vibration wave function of interest. For lower levels whose wave function is localized near the equilibrium distance, the dipole moment can be regarded as being linear (i.e., odd-function-like). Thereby, the TDM  $\mu_{i,i+1}$  between these lower levels increases monotonically as the vibrational level increases, as for the harmonic model. For higher levels, however, such linear approximation of the dipole moment does not hold,

and the nonlinearity of it becomes pronounced. As the bond length increases, the dipole function takes maxima (i.e., even-function-like) and then decreases asymptotically to zero. This behavior results from the relaxation of the molecular polarization, which generally occurs for charge-neutral heteronuclear diatomic molecules. Owing to the even-function nature of the dipole function, the TDM  $\mu_{i,i+1}$  between higher levels decreases as the vibrational level increases. As a consequence, the TDM between certain levels has a near-zero value, as can be seen in Figs. 1(b) and 1(c) for LiH and HF, respectively.

No missing rung will appear in the VLC simulations based on the assumption of the linear dipole function and is likely to give an unrealistic result. Since the position of the missing rung sensitively depends on the shape of the PES and dipole function (see Appendix A), highly accurate quantum chemistry methods are required to identify its exact position.

### III. NUMERICAL EXPERIMENTS

To verify the existence of the missing rung by numerical experiments, we conducted wave-packet dynamics simulations for the LiH molecule. The time evolution of the wave packet  $\Psi(x, t)$  under a laser electric field  $E(t)$  is expressed by the following time-dependent Schrödinger equation:

$$i\hbar \frac{\partial}{\partial t} \Psi(x, t) = H(x, t) \Psi(x, t), \quad (1)$$

where the Hamiltonian  $H(x, t)$  is defined by

$$H(x, t) = H_0(x) - \mu(x)E(t), \quad (2)$$

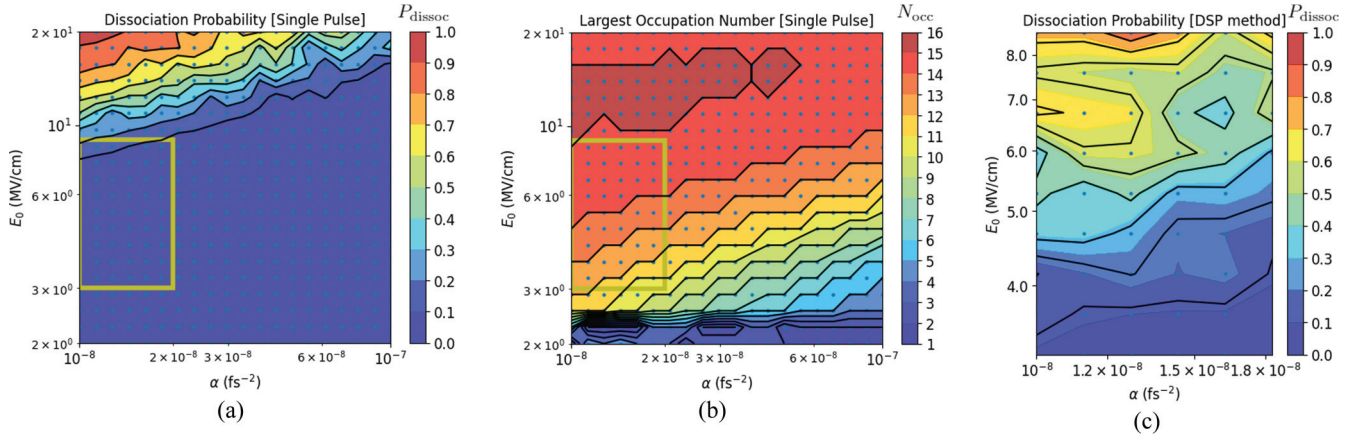


FIG. 2. Color maps of the results of the single-pulse method and the double-stepping pulse (DSP) method (explained later in the paper). (a) Dissociation probabilities  $P_{\text{dissoc}}$  and (b) vibrational level with the largest occupation number  $N_{\text{occ}}$  for the single-pulse method. (c) Dissociation probabilities  $P_{\text{dissoc}}$  for the DSP method. The blue dots represent the grid points where the wave-packet simulations were conducted. The yellow boxed area in (a) and (b) represents the parameter range chosen for the DSP method.

$$H_0(x) = -\frac{\hbar^2}{2M_{\text{red}}} \frac{\partial^2}{\partial x^2} + V(x). \quad (3)$$

$M_{\text{red}}$  in  $H_0(x)$  is the reduced mass of LiH. The potential energy  $V(x)$  and the dipole moment  $\mu(x)$  were calculated by the multireference averaged quadratic coupled-cluster (MR-AQCC) method [27]. Details of these computations are described in Appendix A. We employ a Gaussian pulse as the electric field  $E(t)$  of the pulsed laser:

$$E(t) = E_0 \exp\{-\alpha(t - t_0)^2\} \cos\{\omega(t)(t - t_0)\}, \quad (4)$$

where  $E_0$  is the maximum electric field amplitude,  $\alpha$  is the Gaussian spreading parameter,  $t_0$  is the center time of the pulse, and  $\omega(t)$  is the time-dependent frequency. The time variation of  $\omega(t)$  is assumed to be a linear chirp, and parametrized by the two dimensionless parameters  $\gamma_1$  and  $\gamma_2$  as

$$\omega(t) = \omega_0 \left\{ -(\gamma_1 + \gamma_2) \frac{t - t_0}{4\sigma} + 1 + \frac{\gamma_1 - \gamma_2}{2} \right\}, \quad (5)$$

where  $\sigma = 1/\sqrt{2\alpha}$  is the standard deviation of the Gaussian pulse envelope. Equation (5) means that  $\omega(t)$  is a linear function through two points,  $\omega(t_0 - 2\sigma) = \omega_0(1 + \gamma_1)$  and  $\omega(t_0 + 2\sigma) = \omega_0(1 - \gamma_2)$ . The reference frequency  $\omega_0$  was set to the transition frequency between the ground state and the first excited state [ $\omega_0 = (\epsilon_1 - \epsilon_0)/\hbar$ ]. Based on the above formulation, the VLC process for the LiH molecule was simulated by computing the time evolution of wave packets initially set to the ground state using the second-order Suzuki-Trotter decomposition method.

Here, we discuss the parameter ranges of  $E_0$  and  $\alpha$  that determine the shape of the pulses. As mentioned in the Introduction, there are two types of excitation process mechanisms induced by chirped lasers: quantum ladder climbing and classical autoresonance. Since MRP is a quantum issue that apparently appears when the vibrational levels can be regarded as discrete, the parameter range should be chosen so that quantum ladder climbing occurs. Therefore, using the characterization parameters proposed by Barth *et al.* [16], we estimated the parameter range for quantum ladder climbing

(see Appendix C for details). The parameter range was determined to be  $E_0 = 2.0\text{--}20$  MV/cm and  $\alpha = 10^{-8}\text{--}10^{-7}$  fs $^{-2}$ . For this parameter range of  $E_0$  and  $\alpha$ , a grid of  $20 \times 20$  points on logarithmic scales was defined and wave-packet dynamics simulations were carried out for each grid point. The chirp parameters  $\gamma_1$  and  $\gamma_2$  were optimized by Bayesian optimization so as to maximize the degree of excitation and the dissociation probability. The degree of excitation was evaluated by the expectation value of the occupied states, and the dissociation probability was evaluated by a time integration of the probability density flux of the wave-packet that reaches the dissociation limit. The details of the wave-packet simulations and optimizations are described in Appendixes B and D.

#### IV. RESULTS

Figures 2(a) and 2(b) show the results of the wave-packet dynamics simulations with optimized chirp parameters. The color map in Fig. 2(a) shows the dissociation probabilities, showing the trend that the dissociation probabilities get larger with larger electric fields ( $\propto E_0$ ) and longer pulse widths ( $\propto 1/\sqrt{\alpha}$ ). This result is a natural consequence of the fact that greater dissociation is promoted by a higher pulse energy. The color map in Fig. 2(b) shows the vibrational state that has the largest occupation number (excluding the ground state) after each of the simulations. It can be seen that there is a wide plateau consisting of the 15th and 16th states. The missing rung of LiH is located around the 16th state, indicating that the wave packet was trapped there due to the missing rung during VLC. This result shows that the MRP hinders photodissociation by VLC. Since the MRP occurs for all molecular bonds with polarization, it is important to solve the MRP to achieve photodissociation by VLC.

#### V. DOUBLE-STEPPING PULSE METHOD

Here, we propose the double-stepping pulse (DSP) method as a solution for the MRP. In addition to a conventional pulse for the adjacent transitions ( $\Delta v = \pm 1$ ), the DSP method uses a secondary pulse to achieve transitions of  $\Delta v = \pm 2$ , i.e.,



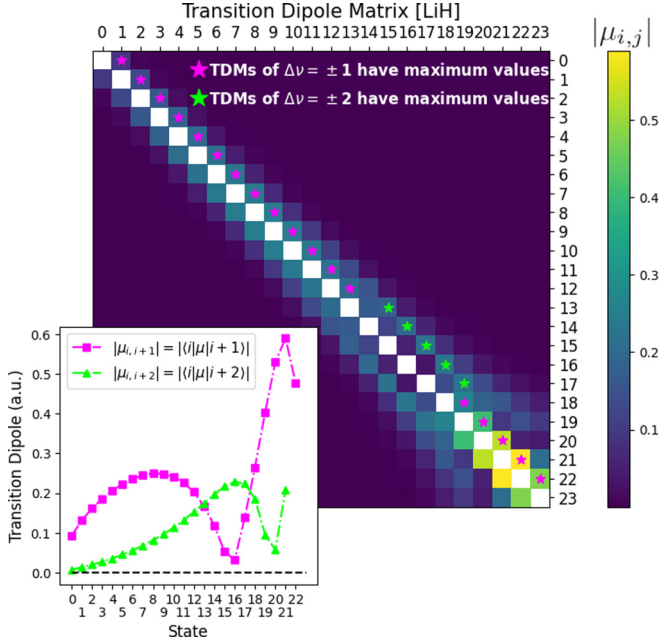


FIG. 3. Absolute values of the transition dipole matrix  $|\mu_{i,j}|$  for the LiH molecule. The star indicates the level where TDM has the maximum value (magenta, TDMs of  $\Delta v = \pm 1$  have maximum values; lime, TDMs of  $\Delta v = \pm 2$  have maximum values). The lower left inset shows the absolute values of TDMs for  $\Delta v = \pm 1$  and  $\Delta v = \pm 2$ . The TDMs are calculated based on the PESs and dipole moments calculated by the MR-AQCC method.

double stepping, between levels around the missing rung. Based on the previous discussion, when the dipole function has an even function property around the missing rung, transitions between levels with different parity ( $\Delta v = \pm 1$ ) are forbidden, while transitions between levels with the same parity ( $\Delta v = \pm 2$ ) are allowed, and vice versa when the dipole function has an odd function property (see Fig. 3). Thereby, the DSP is complementary to a conventional pulse for successful VLC. A well-known ladder climbing method with two pulses is Raman chirped adiabatic passage (RCAP) [7,28,29], which excites vibrational levels with series of Raman pulses (linearly chirped pump and Stokes pulses). The key difference between RCAP and the DSP method is that RCAP uses non-resonant Raman pulses, while the DSP method uses resonant pulses for vibrational excitation.

To show the effectiveness of our method, we conducted wave-packet dynamics simulations of the DSP method. For the main pulse for the transitions of  $\Delta v = \pm 1$  we chose pulse parameters for which almost no dissociation occurred using a single pulse [ $E_0 = 3.0$ - $9.0$  MV/cm,  $\alpha = (1.0$ - $2.0) \times 10^{-8}$  fs $^{-2}$ , and  $9 \times 6$  grid points on logarithmic scales, as shown in the yellow boxed areas in Fig. 2]. For the DSP, the pulse parameters  $E_0 = 3.0$  MV/cm and  $\alpha = 8.0 \times 10^{-8}$  fs $^{-2}$  were used. Here, we have to optimize the chirp parameters for two pulses, the main pulse and the DSP, and the delay time between the two pulses ( $\Delta t_0 = t_0^{\text{main}} - t_0^{\text{DSP}}$ ). Hence, we have to optimize five parameters,  $\gamma_1^{\text{main}}$ ,  $\gamma_2^{\text{main}}$ ,  $\gamma_1^{\text{DSP}}$ ,  $\gamma_2^{\text{DSP}}$ , and  $\Delta t_0$ . Since the computational cost of handling five variables in Bayesian optimization is high, the Covariance Matrix Adaptation Evolution Strategy (CMA-ES) [30] evolutionary

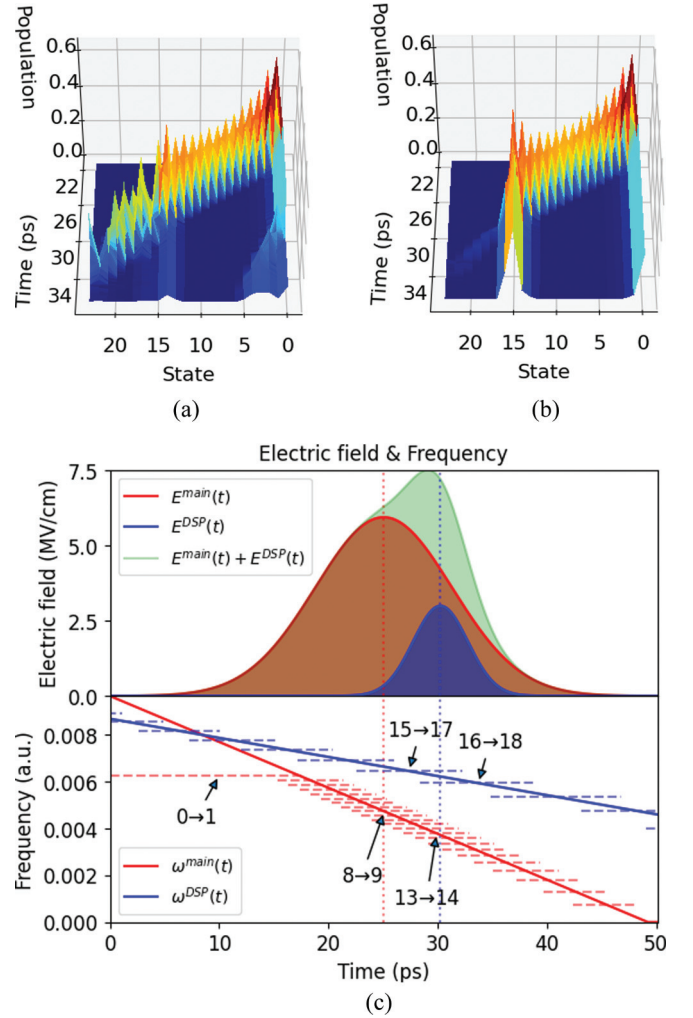


FIG. 4. (a) Snapshot of the excitation process with the most energy efficient pulses in the DSP method. The pulse parameters of the main pulse are  $E_0 = 5.95$  MV/cm and  $\alpha = 1.27 \times 10^{-8}$  fs $^{-2}$ . (b) Snapshot of the excitation process with only the main pulse, with the same parameters as in (a). (c) Top: Electric field intensities of the main pulse, the DSP, and the overall field. Bottom: Corresponding time-dependent frequencies of the main pulse and the DSP in (a). The red and blue dashed lines represent the transition frequencies for  $\Delta v = \pm 1$  (red) and  $\Delta v = \pm 2$  (blue).

optimization method was used for the parameter optimization (see Appendix D for details). The reference frequency of the DSP is set to the transition frequency between the 15th and 17th levels,  $\omega_0^{\text{DSP}} = (\epsilon_{17} - \epsilon_{15})/\hbar$ , where most of the wave packets were trapped, as shown in Fig. 2(b). Although the effect of the relative phase on dissociation probabilities is not negligible, the relative phase between the main pulse and the DSP was set to zero for the ease of optimizations. The effect of the relative phase is discussed in Sec. VI.

The dissociation probabilities obtained by the DSP method are shown in Fig. 2(c). It can be seen that the DSP method enhances the dissociation significantly compared to the single-pulse method [Fig. 2(a)]. Although this result shows the superiority of the DSP method over the single-pulse method in terms of the dissociation probabilities, the energy

efficiency of the DSP method remains a concern because the method requires additional energy to generate the additional pulse. Thus, we compared the energy efficiency of the two methods, specifically the amount of dissociated molecules per unit energy of the pulses. (Details of the calculation method are described in Appendix E.) The highest energy efficiency for the DSP method was 0.763 ) while that for the single-pulse method was 0.193 mol/J. Thus, the DSP method was found to be about four times more efficient than the single-pulse method, demonstrating that the DSP method is a promising method for solving the MRP. This result was obtained based on simulations only for the molecular vibrational degrees of freedom; however, the rotational degrees of freedom need to be taken into account for more realistic simulations. Since the dissociation efficiency may decrease due to the leakage of populations to undesired levels caused by the rovibrational coupling, it may be necessary to use light-induced molecular orientation control techniques [31,32].

Figure 4(a) shows a snapshot of the wave-packet dynamics simulations with the most energy efficient pulses in the DSP method. Figure 4(b) shows a snapshot with only the main pulse in Fig. 4(b). Without the DSP [Fig. 4(b)], it is clearly seen that the wave packet is trapped in the missing rung level, while with the DSP [Fig. 4(a)], the wave packet is successfully excited to the dissociation limit. Figure 4(c) shows the electric fields and time-dependent frequencies used for the above simulation shown in Fig. 4(a). It clearly shows that the DSP is focused on the 15th and 16th excitation frequencies which are around the missing rung. The fluence of the main pulse is 522 mJ/cm<sup>2</sup>, and that of DSP is 53 mJ/cm<sup>2</sup>. The wavelength corresponding to the center frequency of the main pulse is 9.6  $\mu$ m and that of DSP is 7.3  $\mu$ m. These properties can be achieved by focusing a few-microjoule laser pulse generated by differential frequency generation to a cross section of several tens of  $\mu$ m<sup>2</sup>. The chirp rate of the main pulse is  $-8.1 \times 10^{-6}$  fs<sup>-2</sup> and that of DSP is  $-3.4 \times 10^{-6}$  fs<sup>-2</sup> and the corresponding group delays of dispersion (GDD) are  $-6.1 \times 10^4$  and  $-1.5 \times 10^5$  fs<sup>2</sup>, respectively. To achieve these GDD with optical media such as calcium fluoride or fused silica, which have negative group velocity dispersion in the infrared region, a thick medium of about a dozen centimeters will be required. It could also be realized by using multiple scattering by a pair of chirped mirrors [33] or an optical fiber [34] with negative group velocity dispersion in the infrared region. Thus, the proposed method is not considered to be physically infeasible in terms of laser intensity and spectrum.

## VI. DYNAMICS OF VIBRATIONAL TRANSITION PROCESSES

The above discussions were limited to phenomenological cases. To understand the mechanism of the DSP method microscopically, we propose an analysis method that clarifies the dynamics of vibrational transition processes under electric fields. We calculated the time evolution of the wave packet  $\Psi(x, t)$  using the Suzuki-Trotter decomposition method without explicitly treating the information of individual vibrational levels. However, the probability amplitude of each vibrational level is necessary to understand the dynamics of the vibrational excitation process. Thus, the probability amplitudes

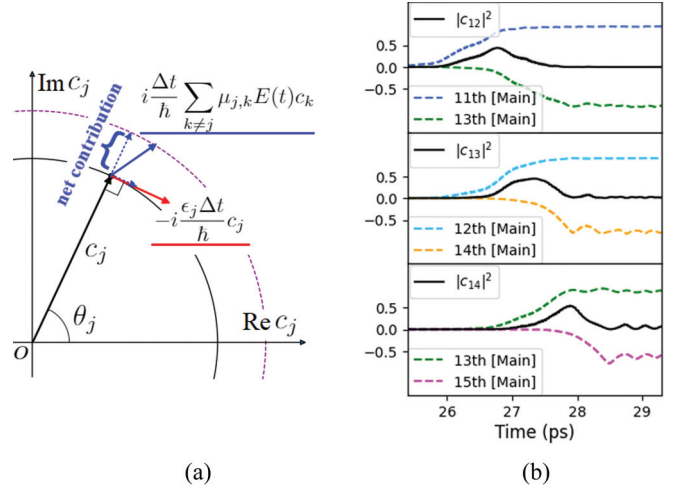


FIG. 5. (a) Schematic illustration of Eq. (7). (b) Occupation numbers  $|c_j|^2(t)$  and the contributions from other levels  $\Delta C_j^{(k)}(t)$  for the 12th, 13th, and 14th levels.

$c_j = \langle \phi_j | \Psi(x, t) \rangle$  of each vibrational level were calculated at each time of the simulation, and the interaction between the vibrational levels is investigated by calculating the off-diagonal elements of the Hamiltonian. Under an arbitrary electric field  $E(t)$ , the time evolution of the probability amplitude  $c_j$  of the  $j$ th level is expressed by the following equation:

$$i\hbar \frac{\partial c_j}{\partial t} = \epsilon_j c_j - \sum_{k \neq j} \mu_{j,k} E(t) c_k, \quad (6)$$

where  $\epsilon_j$  is the eigenenergy of the  $j$ th level and  $\mu_{j,k}$  is the TDM of the  $j$ th and  $k$ th levels. Approximately, the variation of the probability amplitude  $\Delta c_j$  during  $\Delta t$  can be written as

$$\Delta c_j \simeq -i \frac{\epsilon_j \Delta t}{\hbar} c_j + i \frac{\Delta t}{\hbar} \sum_{k \neq j} \mu_{j,k} E(t) c_k. \quad (7)$$

Figure 5(a) illustrates the meaning of Eq. (7). The first term of the right-hand side of Eq. (7) does not change the norm of  $c_j$  since it merely rotates  $c_j$  in the complex plane. On the other hand, the second term, which is the summation of off-diagonal elements of the Hamiltonian and represents the mixing with other levels via the electric field, affects the norm of  $c_j$ . As shown in Fig. 5(a), the radial component of the second term changes the norm of  $c_j$ . Therefore, the contribution to the norm of  $c_j$  can be quantified through rotating  $\Delta c_j$  by the argument of  $c_j$ ,  $\theta_j = \arg c_j$ , and taking its real part. The second term in Eq. (7) can be regarded as the summation of contributions to  $c_j$  from each level. Since the TDM  $\mu_{j,k}$  and probability amplitudes  $c_k$  for each level are obtained, each element of this summation can be calculated. We define  $\Delta C_j^{(k)}(t)$  as the time integration of the contribution to the  $j$ th level from the  $k$ th level, indicating the net contribution of the  $k$ th level to the  $j$ th level norm up to time  $t$ . It is written as

$$\Delta C_j^{(k)}(t) = \int_{-\infty}^t \text{Re} \left( i \frac{\mu_{j,k} E(t')}{\hbar} c_k(t') \exp(-i\theta_j(t')) \right) dt'. \quad (8)$$

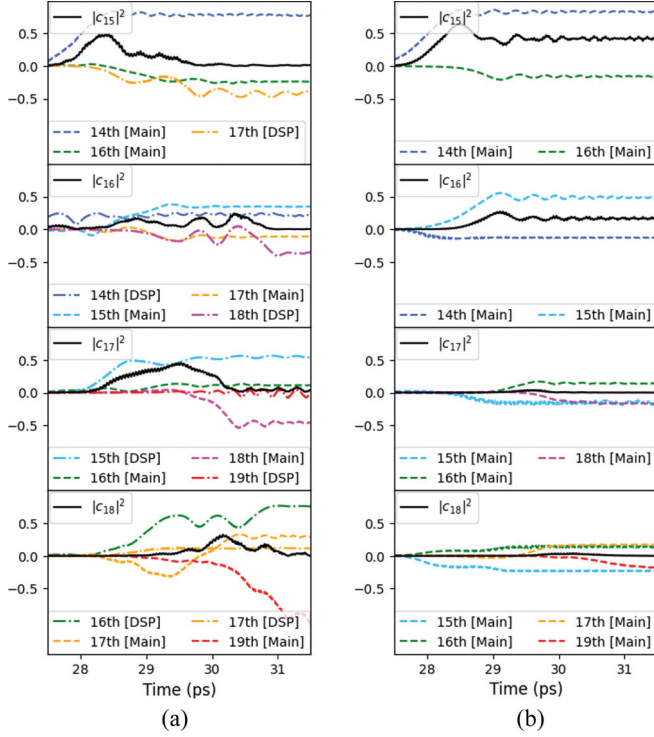


FIG. 6. Occupation numbers  $|c_j|^2(t)$  and contributions from other levels  $\Delta C_j^{(k)}(t)$  for the 15th, 16th, 17th, and 18th levels (a) with DSP and (b) without DSP.

A positive value of Eq. (8) means that the  $k$ th level acts to increase the norm of the  $j$ th level, and a negative value means that it acts to decrease it. By calculating  $\Delta C_j^{(k)}(t)$  for each level, it is possible to analyze which vibrational level has the dominant contribution to the excitation process of a given level. Furthermore, by calculating  $\Delta C_j^{(k)}(t)$  for each electric field component  $E^{\text{Main}}(t)$  and  $E^{\text{DSP}}(t)$ , we can distinguish the contributions of each pulse.

Figure 5(b) shows the occupation number of the 12th, 13th, and 14th vibrational levels (levels lower than the missing rung) and the contribution from the other levels calculated by Eq. (8) for the simulation of the DSP method shown in Fig. 4(a). It can be understood that the cascade excitation of a wave packet, i.e., VLC, is the result of quantum interference of the positive contribution from the lower level and the slightly delayed negative contribution from the upper level. Note that these transitions are caused by contributions from adjacent levels, which agree with the process of quantum ladder climbing described by successive Landau-Zener transitions [16]. It is also worth noting that even though the electric field of the DSP is present during the transition of these levels, it does not contribute at all to the changes in occupation numbers. This indicates that the excitation processes at levels lower than the MRP region are all induced by the main pulse. Next, we show the results for the vibrational levels of the 15th, 16th, 17th, and 18th (levels around the missing rung) in Fig. 6. Figure 6(a) shows the result with DSP shown in Fig. 4(a) and Fig. 6(b) shows the result without DSP shown in Fig. 4(b). Comparing the time variations of the occupation number for the 15th level, it can be seen that without the DSP, the positive

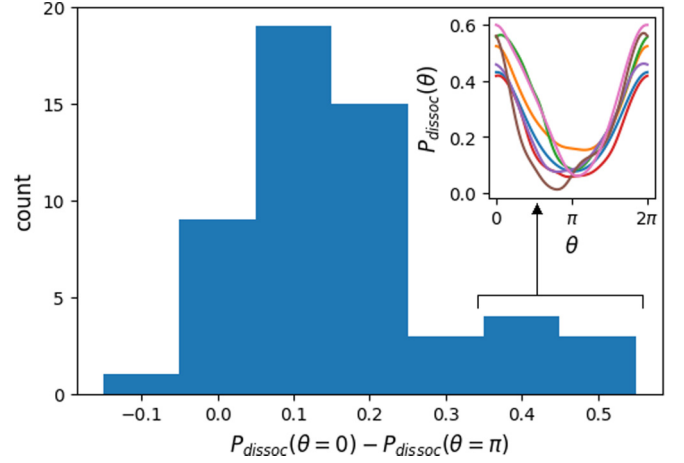


FIG. 7. Histogram of the values of the difference between the dissociation probability at relative phase  $\theta = 0$  [ $P_{\text{dissoc}}(\theta = 0)$ ] and  $\theta = \pi$  [ $P_{\text{dissoc}}(\theta = \pi)$ ]. The inset shows the relationships between the dissociation probabilities and relative phases for pulses of  $P_{\text{dissoc}}(\theta = 0) - P_{\text{dissoc}}(\theta = \pi) \geq 0.35$ .

contribution of the 14th level is not sufficiently canceled by the negative contribution from the 16th level, and most of the wave packet remains in the 15th level, whereas with the DSP, the additional negative contribution from the 17th level caused by the DSP significantly decreases the occupation number of the 15th level. In the contribution to the 17th level in Fig. 6 there are slight contributions from other levels without the DSP. On the other hand, there is an apparent positive contribution from the 15th level with the DSP, which excites wave packets to higher levels. Such an interlevel excitation can also be seen between the 16th and 18th levels for the DSP method. These results confirm the interpretation of the MRP and the mechanism of the DSP method.

The proposed contributions reveal that the DSP method utilizes quantum interference effectively to solve the MRP. Such quantum interference effects are one of the most important features of coherent control [35–37]. Another indication of quantum interference is the effects of the phases of the electric fields. For the 54 pulses considered in the DSP method with optimized parameters at a relative phase of zero, we performed a wave-packet dynamics simulation by varying the relative phases from zero to  $2\pi$ .

Figure 7 shows the histogram of the values of the difference of the dissociation probability at relative phase  $\theta = 0$  [ $P_{\text{dissoc}}(\theta = 0)$ ] and  $\theta = \pi$  [ $P_{\text{dissoc}}(\theta = \pi)$ ]. For many pulses, it is found that the dissociation probability differs significantly between  $\theta = 0$  and its antiphase,  $\theta = \pi$ . This result implies that the phases of the electric field and that of the vibrational levels are coupled, and they play an important role in the dynamics of quantum interference between vibrational levels. Thus, the quantum interference effect is deeply related to the DSP method. The inset of Fig. 7 shows the relationship between the dissociation probability and relative phases for pulses of  $P_{\text{dissoc}}(\theta = 0) - P_{\text{dissoc}}(\theta = \pi) \geq 0.35$ . The dependencies between dissociation probabilities and relative phases show distorted cosine functional curves. Since the pulse parameters were optimized with relative phase



$\theta = 0$ , it is reasonable that they exhibit a cosine functional shape which takes a maximum value at  $\theta = 0$ . However the dissociation probability is a resulting value from the complicated interaction between the coupled vibrational levels coupled with the electric field, its dependency is not considered to be expressed by a simple cosine function. The distortion of the cosine function can be attributed to complicated interferences between vibrational levels, but complete understanding of these functional shapes needs further investigation.

## VII. SUMMARY

In summary, we simulated photodissociations by VLC based on the PES and dipole moment computed by a highly accurate quantum chemistry method. We found the MRP, which causes an interruption of VLC, and revealed that the MRP is caused by the disappearance of the adjacent TDM at a specific vibrational level. As a solution to this problem, we proposed the DSP method that uses additional pulses to induce a  $\Delta v = \pm 2$  transition, and verified its effect on the MRP by wave-packet dynamics simulations. We note that the DSP method not only enhances the dissociation probability but is also more energy efficient than the single-pulse method. We also clarified the detailed mechanisms of VLC and the DSP method. The excitation process of VLC is caused by quantum interference between the positive contribution from the lower level and the negative contribution from the upper level and the DSP plays an essential role in the excitation process to higher levels. The MRP is considered to be a ubiquitous problem in VLC because it originates in the parity of the vibrational wave function and the dipole function. The MRP may be why there are few experimental reports of VLC-induced molecular bond breaking, and we believe that our findings may pave the way to VLC-induced photodissociation and, ultimately, to the versatile control of chemical reactions.

## APPENDIX A: QUANTUM CHEMISTRY COMPUTATIONS

The potential energy curves and dipole moments of the LiH and HF molecules were calculated using the multireference averaged quadratic coupled-cluster (MR-AQCC) method [27]. First, complete active space self-consistent field (CASSCF) calculations [38] were carried out and the obtained CASSCF wave functions were adopted as reference functions for the MR-AQCC calculations. For LiH, the molecular orbitals derived from the Li 2s and H 1s atomic orbitals were selected as active orbitals. The complete active space (CAS) was constructed by distributing two electrons over these two orbitals. In the MR-AQCC calculations, the electrons in Li 1s were additionally correlated. For HF, the molecule was placed on the  $z$  axis. Accordingly, the H 1s and F 2p $z$  orbitals were relevant for the formation of the H-F bond. The molecular orbitals derived from these atomic orbitals were selected as active orbitals in the CASSCF calculations; two electrons involved in these orbitals were treated as active electrons. The electrons in the orbitals originating from F 1s, F 2s, F 2p $x$ , and F 2p $y$  were also correlated in the MR-AQCC calculations. The basis set used was Dunning's aug-cc-pVQZ [39–41].

TABLE I. Calculated and experimental parameters for LiH and HF.  $r_e$  are the equilibrium distances,  $D_0$  are the dissociation energies,  $\omega_e$  are the fundamental vibrational frequencies, and  $\mu$  are the dipole moments.

System	$r_e$ (Å)	$D_0$ (eV)	$\omega_e$ (cm <sup>-1</sup> )	$\mu$ (debye)
LiH (calc.)	1.5710	2.496	1422.22	5.792
LiH (expt.)	1.5957	2.429	1405.65	5.882
HF (calc.)	0.9168	5.848	4103.48	1.791
HF (expt.)	0.9168	5.869	4138.32	1.826

All the calculations were carried out using the GAMESS program [42,43]. The calculated spectroscopic parameters and dipole moments are summarized in Table I. Here, the spectroscopic parameters were estimated by fitting the potential energy curve with a quadratic function. The calculated parameters were in good agreement with the corresponding experimental values [44]. The results suggest that the potential energy curves and dipole moments are reliable over the entire range. The CASSCF and MR-AQCC potential energy curves and transition dipole moments are compared in Fig. 8. The CASSCF results were quite different from the MR-AQCC results because of the lack of dynamical correlations. As a result, the missing rung in which the transition dipole moment is close to zero appeared at different states. The results suggest that calculations using a high-level method are necessary to estimate the exact position of the missing rung.

## APPENDIX B: WAVE-PACKET DYNAMICS SIMULATIONS

Nonrelativistically, the time evolution of quantum systems can be described by the time-dependent Schrödinger equation,

$$i\hbar \frac{\partial}{\partial t} \psi(x, t) = H(t) \psi(x, t). \quad (\text{B1})$$

The formal solution of the Schrödinger equation with the time-independent potential  $V(x)$  can be written as

$$\psi(x, t) = e^{-i\frac{H(x)}{\hbar}t} \psi(x, 0), \quad (\text{B2})$$

where  $U(t) = e^{-i\frac{H(x)}{\hbar}t}$  is the time-evolution operator. However, we have to consider the time-dependent Hamiltonian  $H(x, t)$  that describes the system under the laser electric field  $E(t)$ ,

$$H(x, t) = -\frac{\hbar^2}{2M} \frac{\partial^2}{\partial x^2} + V(x, t), \quad (\text{B3})$$

where  $V(x, t) = V(x) - \mu(x)E(t)$ . To treat the time-varying potential  $V(x, t)$ , we set  $t = Ndt$  and express the time evolution operator as the product of  $N$  operators in time increments of  $dt$ ,

$$U(t) = \prod_{j=0}^N U_j(dt), \quad (\text{B4})$$

where

$$U_j(dt) = e^{-i\frac{H(x, jdt)}{\hbar}dt}. \quad (\text{B5})$$

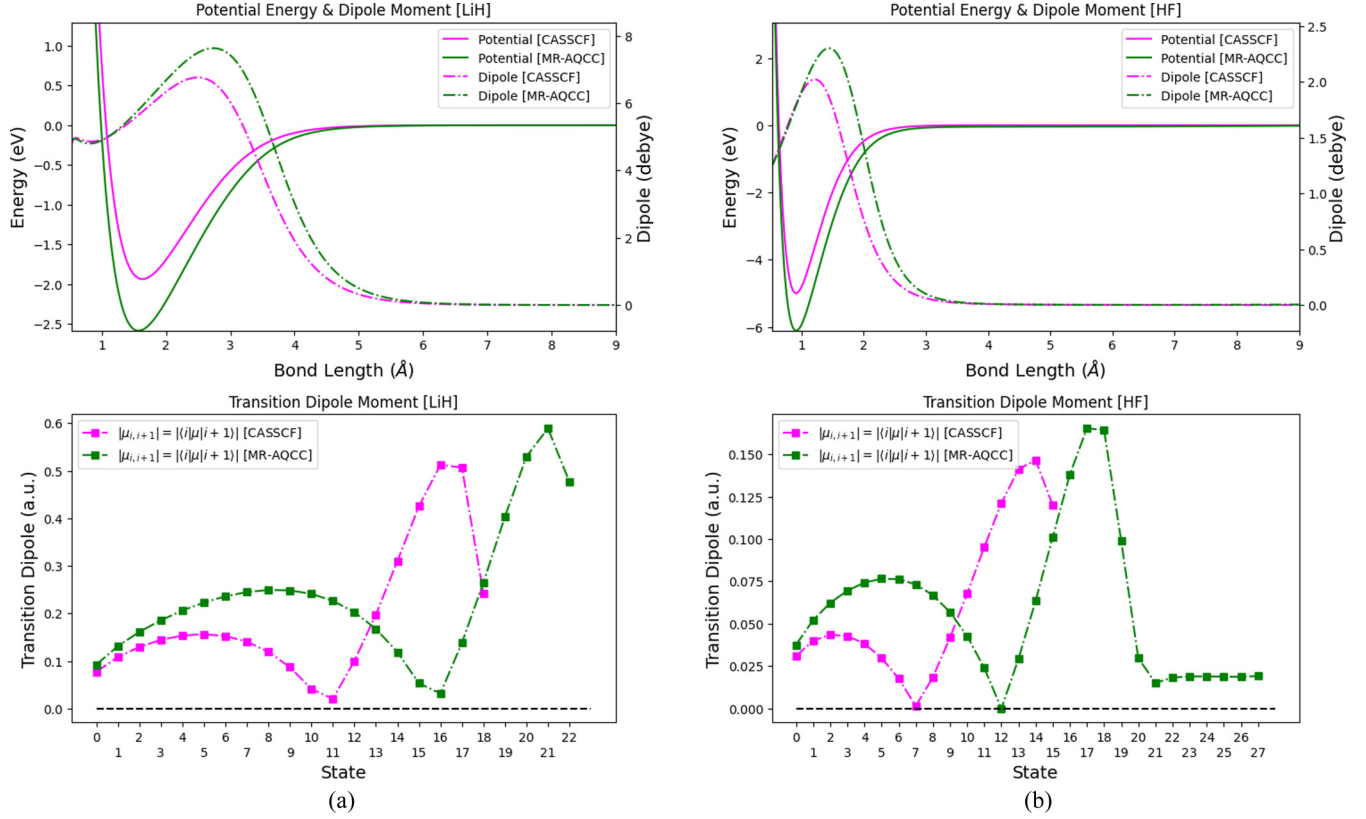


FIG. 8. Comparison between CASSCF and MR-AQCC. Top: PESs and dipole moments for (a) LiH molecule and (b) HF molecule. Bottom: Absolute values of the corresponding TDMs.

Several methods of applying an exponential operator to a wave function have been developed [45], including methods based on a Taylor expansion and the Chebyshev-polynomial method. However, the Suzuki-Trotter decomposition method [46,47] is often used because of the good balance between computational cost and speed. We also use the Suzuki-Trotter decomposition method for the time-evolution computation. The second-order Suzuki-Trotter decomposition can be written as

$$U_j(dt) \sim e^{-i\frac{T}{\hbar} \frac{dt}{2}} e^{-i\frac{V(x, jdt+dt/2)}{\hbar} dt} e^{-i\frac{T}{\hbar} \frac{dt}{2}} + O(dt^3). \quad (\text{B6})$$

An error arises because  $T$  and  $V$  are noncommutative. Here,  $T$  is diagonal in wave-number space and  $V$  is diagonal in real space, so in the second-order Suzuki-Trotter method, when applying  $e^{-i\frac{T}{\hbar} \frac{dt}{2}}$ , the wave function is expressed in wave-number space using a fast Fourier transform (FFT) and  $e^{-i\frac{V(x, jdt+dt/2)}{\hbar} dt}$  is applied to the wave function, which returns to real-space notation by an inverse FFT. When  $e^{-i\frac{T}{\hbar} \frac{dt}{2}}$  is applied again, the wave function is expressed in wave-number space using the FFT again. Using the above procedure, the time-evolution computation can proceed without expanding the exponential function operator. By repeating these calculations  $N$  times, the wave function at the desired time  $t$  can be obtained. For the simulations of LiH dissociation by chirped laser pulses,  $dt = 1.0$  a.u. is used. The simulation time  $\tau_{\text{sim}}$  depends on the shape of the chirped laser pulses,  $\tau_{\text{sim}} = 8\sigma$ , where  $\sigma$  is the standard deviation of the Gaussian envelope for the pulse laser. We take an evenly spaced isotropic grid of

$2^{10}$  elements for  $x$  in the range  $x = 1.5$ -15.0 bohrs. Figure 9 shows several vibrational wave functions represented in wave-number space, indicating that the wave-number space (and corresponding number of grids) is sufficient to represent the wave function of the bound state.

### 1. Dissociation probability

Here, we describe how to calculate the dissociation probability. The wave functions that reach the right edge of the

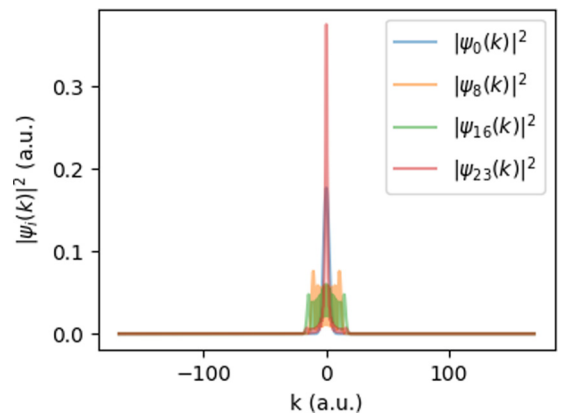


FIG. 9. Vibrational wave functions represented in wave-number space corresponding to a grid of  $2^{10}$  elements for  $x$  in the range  $x = 1.5$ -15.0 bohrs.



grid represent the state of bond dissociation. Therefore, the probability densities  $|\psi(x_{\text{right-edge}})|^2$  represent the dissociation probability. It is convenient to use the probability density flux,

$$\begin{aligned} J(x, t) &= \frac{\hbar}{2iM} \{ \psi^*(x, t) \nabla \psi(x, t) - (\nabla \psi(x, t))^* \psi(x, t) \} \\ &= \text{Re} \left\{ \psi(x, t)^* \frac{\hbar}{iM} \nabla \psi(x, t) \right\}. \end{aligned} \quad (\text{B7})$$

$\frac{\hbar}{iM} \nabla \psi(x, t)$  can be transformed as the following:

$$\frac{\hbar}{iM} \nabla \psi(x, t) = \hat{p} \psi(x, t) / M = \text{IFFT}(k \psi(p, t)) / M, \quad (\text{B8})$$

where IFFT means an inverse FFT. Thereby we can quickly compute  $\frac{\hbar}{iM} \nabla \psi(x, t)$  because we have the wave function in wave-number space  $\psi(p, t)$  and can therefore use the Suzuki-Trotter decomposition method for the time-evolution computation. The time integral of the probability density flux at the right edge of the grid after a sufficiently long simulation time gives the dissociation probability in this case:

$$P_{\text{dissoc}} = \int_0^{\tau_{\text{sim}}} J(x_{\text{right-edge}}, t') dt'. \quad (\text{B9})$$

## 2. Complex absorbing potential

An absorption potential with a negative pure imaginary value was set to prevent the wave function from reaching the grid boundary. Here, we used the complex absorption potential of a fourth-order function,

$$V_{\text{absorb}}(x) = -i\xi x^4, \quad (\text{B10})$$

where  $\xi = 1.0$  is used in this study. The norm of the wave function reaching the region where this function has a significant value decays. This prevents reflections at the edge and the consequent unwanted interference. We placed the potential just after the flux calculation point.

## APPENDIX C: RANGE OF LASER PARAMETERS

Since the MRP is a quantum problem that appears when the vibrational levels can be regarded as being discrete, we have to choose laser parameters ( $E_0$ , maximum electric field amplitude, and  $\alpha$ , Gaussian spreading parameter) that reproduce the excitation process where quantum phenomena are dominant. Here, we provide a rough estimation of the laser parameter range where quantum ladder climbing occurs, using the parameters proposed by Barth *et al.* to distinguish between quantum ladder climbing and classical autoresonance [16].

The excitation process is characterized by three time scales,  $T_R = \sqrt{2m\hbar\omega_0}/\Lambda$  (the Rabi time scale),  $T_S = 1/\sqrt{\Gamma}$  (the sweep rate time scale), and  $T_{\text{NL}} = 2\omega_0\beta/\Gamma$  (the nonlinear transition time scale), where  $m$  is the reduced mass,  $\omega_0$  is the eigenfrequency,  $\beta$  is the anharmonicity of the system,  $\Lambda$  is the driving amplitude (amplitude of the oscillatory component of the Hamiltonian), and  $\Gamma$  is the chirp rate. To obtain the values of  $\omega_0$  and  $\beta$  of LiH, the excitation frequency is fitted with the following equation:

$$\omega_{n,n+1} = \omega_0 \{1 - 2\beta(n+1)\}. \quad (\text{C1})$$

The fitting gives  $\omega_0 = 0.0068$  a.u.,  $\beta = 0.0176$ . The driving amplitude  $\Lambda$  corresponds to the product of the electric field

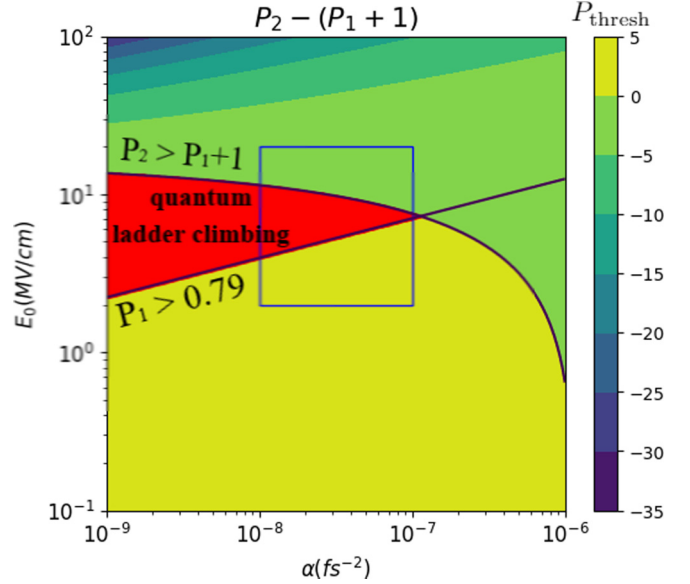


FIG. 10. Characterization parameter  $P_{\text{thresh}} = P_2 - (P_1 + 1)$  calculated in the ranges  $E_0 = 10^{-1}$ - $10^2$ ,  $\alpha = 10^{-9}$ - $10^{-6}$ . The parameter range corresponding to the quantum ladder climbing is colored red. The blue boxed area represents the parameter ranges we chose.

and the linear dipole moment. Although the dipole moment of LiH is nonlinear, in the range 2–5.5 bohrs, it is linearly approximated to be  $\mu(x) \simeq 0.354x + 1.086$ . The effective driving amplitude  $\Lambda^{\text{eff}}$  is estimated as  $\Lambda^{\text{eff}} = 0.354E_0$ . The chirp rate  $\Gamma$  is taken as the value when  $\gamma_1 = \gamma_2 = 0.5$ , namely,  $\Gamma = \omega_{0 \rightarrow 1}/4\sigma$ .

Based on these values,  $T_R$ ,  $T_S$ , and  $T_{\text{NL}}$  are calculated. The parameters that distinguish the quantum case from the classical case  $P_1, P_2$  are expressed as follows:

$$P_1 = \frac{T_S}{T_R}, \quad (\text{C2})$$

$$P_2 = \frac{T_{\text{NL}}}{T_S}. \quad (\text{C3})$$

The conditions under which phase-locked ladder climbing occurs are as follows:

$$P_2 > P_1 + 1, \quad (\text{C4})$$

$$P_1 > 0.79. \quad (\text{C5})$$

Figure 10 shows the calculated value of  $P_{\text{thresh}} = P_2 - (P_1 + 1)$  for the parameter ranges  $E_0 = 10^{-1}$ - $10^2$ ,  $\alpha = 10^{-9}$ - $10^{-6}$ . The parameter range that satisfies conditions (C4) and (C5) is colored in red. From Fig. 10, ladder climbing is considered to occur in the parameter range  $E_0 = 2.0$ - $20$  MV/cm,  $\alpha < 10^{-7}$  fs $^{-2}$ . It is not possible to make  $\alpha$  arbitrarily small due to the vibrational relaxation time. Although there are two types of vibrational relaxation, intra- and intermolecular vibrational relaxation, only intermolecular vibrational relaxation is considered in estimating the vibrational relaxation time. Intramolecular vibrational relaxation (IVR) will be negligible because the LiH molecule is a small molecule and IVR will be suppressed by the phase locking (or “photon locking”) between the chirped electric field and vibrational

states [48–51]. The intermolecular vibrational relaxation time of LiH is estimated using the mean free time of LiH at standard state (298.15 K and  $10^5$  Pa). The mean free time depends on the molecular radius, which varies significantly during the dissociation process. Assuming that the molecular radius is half the equilibrium distance ( $r_e \simeq 1.6$  Å), the mean free time is 377 ps. The tail of the wave function of the highest bound state reaches about 5 Å, and assuming the molecular radius is half this distance, the mean free time is 39 ps. Thus, the time scale for vibrational relaxation is estimated to be several tens of picoseconds, which corresponds to the parameter range  $\alpha = 10^{-8}$ - $10^{-7}$  fs $^{-2}$ .

Based on the above estimation, we set the parameter ranges as  $E_0 = 2.0$ - $20$  MV/cm,  $\alpha = 10^{-8}$ - $10^{-7}$  fs $^{-2}$  (blue boxed area in Fig. 10). Note that a more detailed discussion is required for an actual system to obtain a more accurate characterization.

#### APPENDIX D: OPTIMIZATION OF THE CHIRPED LASER PULSE PARAMETERS

Here, we describe the details of the optimization methods of chirped laser parameters. We adopted the following linear chirped frequency as the time-dependent frequency  $\omega(t)$  of the laser pulse:

$$\omega(t) = \omega_0 \left\{ -(\gamma_1 + \gamma_2) \frac{t - t_0}{4\sigma} + 1 + \frac{\gamma_1 - \gamma_2}{2} \right\}. \quad (\text{D1})$$

Equation (D1) is parametrized by the two dimensionless parameters  $\gamma_1$  and  $\gamma_2$ . These chirp parameters significantly affect the excitation process of VLC. To achieve a more effective excitation, we optimized these parameters using a combination of machine learning and a wave-packet dynamics simulation. We used machine learning to update the parameters based on the evaluated values of the parameters obtained by the wave-packet dynamics simulation.

For a single pulse, the two parameters  $\gamma_1$  and  $\gamma_2$  are optimized in a range restricted to  $[0,1]$  so as to represent the down-chirp. This parameter space is divided into a  $100 \times 100$  grid (i.e., 0.01 steps), and the optimal parameter is searched from these grid points by the optimization method.

The chirp parameters are optimized for each of 400 different pulses; thus a fast and efficient optimization method is required. In addition, since the effects of the parameters on the excitation process cannot be evaluated analytically, this system is regarded as a black box. As a fast black-box optimization method, we employed Bayesian optimization. Bayesian optimization enables efficient exploration and optimization in parameter space leveraging predictive models such as Gaussian process regression, which is a powerful method for black-box optimization [52]. We used Gpy [53], an open source library in PYTHON, for the implementation of Bayesian optimization. In the optimization, we adopted Gaussian process regression with the radial basis function (RBF) kernel as the predictive model for the parameter space, and employed the upper confidential bound (UCB) as the acquisition function. The iteration number for updating parameters was set to 50.

The objective function was set to be the sum of the excited and dissociated wave packets. Although we aim to find pa-

rameters that give efficient photodissociation, for some pulse parameters whose energy is not sufficient to cause dissociation, an objective function with only an amount of dissociation will result in insufficient optimization. Therefore, by including an amount of an excited wave packet in the objective function in addition to the dissociated wave packet, it is possible to obtain optimized parameters that realize efficient excitation. The amount of dissociated wave packet is evaluated by integrating the absorbed wave packet described in the previous section. The degree of excitation is evaluated by the expected value of the occupied states  $|\phi_j\rangle$ , as follows:

$$P_{\text{excited}} = \sum_{j=0}^{n_{\text{dissoc}}} \left( \frac{j}{n_{\text{dissoc}}} \right) |\langle \phi_j | \psi(x, t) \rangle|^2, \quad (\text{D2})$$

where  $n_{\text{dissoc}}$  is the highest level in the bound state,  $n_{\text{dissoc}} = 23$  in the case of LiH. The expected value of the level is normalized by  $n_{\text{dissoc}}$  in order to balance the amount of dissociation, whose value range is  $[0,1]$ . Based on the above settings, optimization of the chirp parameters was performed for a single pulse.

In the case of the DSP method, there are five parameters to be optimized: the chirp parameters of the main pulse and the DSP,  $\gamma_1^{\text{Main}}$ ,  $\gamma_2^{\text{Main}}$ ,  $\gamma_1^{\text{DSP}}$ , and  $\gamma_2^{\text{DSP}}$ , and the delay time between the main pulse and the DSP ( $\Delta t_0 = t_0^{\text{DSP}} - t_0^{\text{Main}}$ ).

Since the computational cost of Bayesian optimization increases in proportion to the cube of the number of variables [54], it is difficult to handle five variables in Bayesian optimization. Thus, CMA-ES [30] was used for optimization. CMA-ES adaptively updates and optimizes the covariance matrix of the multivariate normal distribution that generates candidate solutions based on the evaluation values of the candidates. It is known that CMA-ES is a robust method that can be optimized even in noisy high-dimensional parameter spaces [55,56].

In the optimization using CMA-ES, the number of generations was set to 150 and the number of individuals to 16 for each generation. The objective function was set to be only the dissociated wave packet because a certain amount of dissociation can be expected by adding the DSP. The initial values  $\gamma_1^{\text{Main}}$  and  $\gamma_2^{\text{Main}}$  are inherited from the optimal parameters for the single-pulse case. The value range of the parameters is not restricted, allowing the parameters to be negative. Negative parameters give the possibility of up-chirping or the DSP reaching ahead of the main pulse.

In this study, the general mathematical optimization algorithms, Bayesian optimization and CMA-ES, were employed for optimizations of pulse parameters. Another option to obtain the optimal external field is the quantum optimal control theory (QOCT) [57], which is one of the most powerful methods in quantum state control. Since QOCT optimizes the instantaneous electric field, it has the potential to obtain a truly optimal electric field waveform, but the resulting electric field and spectrum tend to be complicated. In order to guarantee the physical feasibility of the pulse, a few numbers of parameters that define the feasible pulse shape (i.e., linearly chirped Gaussian pulse) were optimized using general mathematical optimization methods instead of using QOCT. It is also possible to optimize the electric field directly by QOCT without restricting the pulse shape to that specified by a few

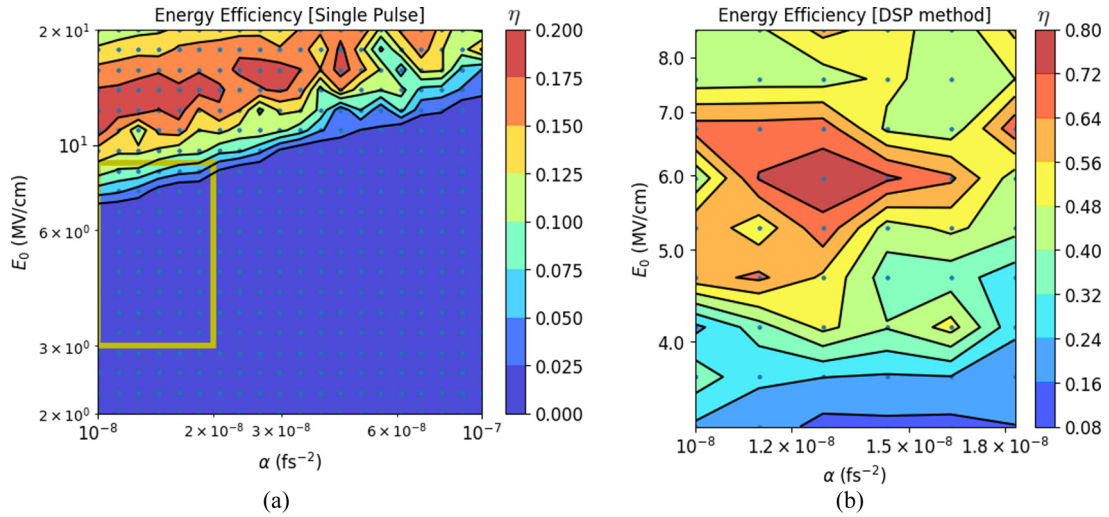


FIG. 11. Calculated energy efficiencies  $\eta$  for (a) a single pulse and (b) the DSP method.

parameters, which may give pulses similar to the DSP method or suggest new strategies for overcoming the MRP.

#### APPENDIX E: ESTIMATION OF ENERGY EFFICIENCY

To determine the energy efficiency of photodissociation by VLC, the energy of the laser pulse and the amount of dissociated molecules have to be estimated. Here, we show a rough estimation of these values. First, we explain how to estimate the energy of a pulse. The electric field of a Gaussian pulsed laser  $E(t)$  is determined by the maximum electric field amplitude  $E_0$  and the Gaussian spreading parameter  $\alpha$  as follows:

$$E(t) = E_0 \exp\{-\alpha(t - t_0)^2\} \cos\{\omega(t)(t - t_0)\}. \quad (\text{E1})$$

The irradiance  $I$  (in  $\text{W}/\text{cm}^2$ ) of a pulsed laser is expressed using the maximum electric field amplitude  $E_0$  (in  $\text{V}/\text{cm}$ ) as follows [58]:

$$I(t) = \frac{c\epsilon_0 n}{2} E(t)^2, \quad (\text{E2})$$

where  $c$ ,  $\epsilon_0$ , and  $n$  are the speed of light, the dielectric constant, and the refractive index of the vacuum, respectively. The energy of a pulse,  $\xi$  (in J), is expressed by the irradiance  $I$  (in  $\text{W}/\text{cm}^2$ ) and cross section of the pulse,  $S$  (in  $\text{cm}^2$ ), as follows:

$$\xi = S \int_{-\infty}^{\infty} I(t) dt = \sqrt{\frac{\pi}{2}} \frac{c\epsilon_0 n}{2} \frac{E_0^2 S}{\sqrt{\alpha}}. \quad (\text{E3})$$

In the case of a single pulse, the total energy required to cause VLC is calculated by Eq. (E3). In the case of the DSP method, two pulses, the main pulse and the DSP, are required for VLC. We assume that the optical system for the implementation of the DSP method is like that used in pump-probe spectroscopy

with a single light source. Assuming that there is no energy loss in such an optical system, the total energy required for VLC becomes the sum of the main pulse and the DSP energy. Since this is a very rough estimate, it is considered that more energy is required for the DSP method in practice.

Next, we explain the calculation method for the amount of dissociated molecules. The number of molecules,  $N_{\text{all}}$  (in moles), present in the region of the pulse cross section  $S$  (in  $\text{cm}^2$ ), can be written as  $N_{\text{all}} = \rho S$ , where  $\rho$  (in  $\text{mol}/\text{cm}^2$ ) is the areal density of the molecules. Assuming that the laser pulse causes dissociation with a dissociation probability  $P_{\text{dissoc}}$ , the number of dissociated molecules,  $N_{\text{dissoc}}$  (in moles), is given by

$$N_{\text{dissoc}} = N_{\text{all}} P_{\text{dissoc}} = \rho S P_{\text{dissoc}}. \quad (\text{E4})$$

For simplicity, we assume that  $\rho = 1 \text{ mol}/\text{cm}^2$ . From Eqs. (E3) and (E4), the energy efficiency  $\eta$  (in  $\text{mol}/\text{J}$ ) of photodissociation by VLC can be estimated as follows:

$$\eta = \frac{N_{\text{dissoc}}}{\xi} = \sqrt{\frac{2}{\pi}} \frac{2}{c\epsilon_0 n} \frac{P_{\text{dissoc}} \sqrt{\alpha}}{E_0^2}. \quad (\text{E5})$$

Based on the above formulation, we estimated the energy efficiency for the results of the single-pulse case and DSP method, respectively.

Figure 11 shows the calculated energy efficiency of each case. It can be seen that the DSP method shows a higher energy efficiency than the single-pulse case. The maximum energy efficiency for a single pulse is  $0.193 \text{ mol}/\text{J}$ , while that for the DSP method is  $0.763 \text{ mol}/\text{J}$ , which is about four times higher. This result shows the superiority of the DSP method with respect to energy efficiency.

[1] P. Brumer and M. Shapiro, Control of unimolecular reactions using coherent light, *Chem. Phys. Lett.* **126**, 541 (1986).

[2] D. J. Tannor and S. A. Rice, Control of selectivity of chemical reaction via control of wave packet evolution, *J. Chem. Phys.* **83**, 5013 (1985).



- [3] T. Baumert, M. Grosser, R. Thalweiser, and G. Gerber, Femtosecond Time-Resolved Molecular Multiphoton Ionization: The Na<sub>2</sub> System, *Phys. Rev. Lett.* **67**, 3753 (1991).
- [4] E. Potter, J. Herek, S. Pedersen, Q. Liu, and A. Zewail, Femtosecond laser control of a chemical reaction, *Nature (London)* **355**, 66 (1992).
- [5] Y. Hikosaka, T. Kaneyasu, M. Fujimoto, H. Iwayama, and M. Katoh, Coherent control in the extreme ultraviolet and attosecond regime by synchrotron radiation, *Nat. Commun.* **10**, 1 (2019).
- [6] H. Goto, H. Katsuki, H. Ibrahim, H. Chiba, and K. Ohmori, Strong-laser-induced quantum interference, *Nat. Phys.* **7**, 383 (2011).
- [7] S. Chelkowski and G. N. Gibson, Adiabatic climbing of vibrational ladders using Raman transitions with a chirped pump laser, *Phys. Rev. A* **52**, R3417 (1995).
- [8] I. Morichika, K. Murata, A. Sakurai, K. Ishii, and S. Ashihara, Molecular ground-state dissociation in the condensed phase employing plasmonic field enhancement of chirped mid-infrared pulses, *Nat. Commun.* **10**, 1 (2019).
- [9] D. Maas, D. Duncan, A. Van der Meer, W. Van der Zande, and L. Noordam, Vibrational ladder climbing in NO by ultrashort infrared laser pulses, *Chem. Phys. Lett.* **270**, 45 (1997).
- [10] G. Marcus, A. Zigler, and L. Friedland, Molecular vibrational ladder climbing using a sub-nanosecond chirped laser pulse, *Europhys. Lett.* **74**, 43 (2006).
- [11] M. Jewariya, M. Nagai, and K. Tanaka, Ladder Climbing on the Anharmonic Intermolecular Potential in an Amino Acid Microcrystal via an Intense Monocycle Terahertz Pulse, *Phys. Rev. Lett.* **105**, 203003 (2010).
- [12] W.-K. Liu, B. Wu, and J.-M. Yuan, Nonlinear Dynamics of Chirped Pulse Excitation and Dissociation of Diatomic Molecules, *Phys. Rev. Lett.* **75**, 1292 (1995).
- [13] W.-K. Liu, J.-M. Yuan, and S. H. Lin, Classical dynamics of multiphoton excitation and dissociation of diatomic molecules by infrared laser pulses, *Phys. Rev. A* **60**, 1363 (1999).
- [14] Y. Duan, W.-K. Liu, and J.-M. Yuan, Classical dynamics of ionization, dissociation, and harmonic generation of a hydrogen molecular ion in intense laser fields: A collinear model, *Phys. Rev. A* **61**, 053403 (2000).
- [15] G. Marcus, L. Friedland, and A. Zigler, From quantum ladder climbing to classical autoresonance, *Phys. Rev. A* **69**, 013407 (2004).
- [16] I. Barth, L. Friedland, O. Gat, and A. G. Shagalov, Quantum versus classical phase-locking transition in a frequency-chirped nonlinear oscillator, *Phys. Rev. A* **84**, 013837 (2011).
- [17] I. Barth and L. Friedland, Quantum Phenomena in a Chirped Parametric Anharmonic Oscillator, *Phys. Rev. Lett.* **113**, 040403 (2014).
- [18] T. Armon and L. Friedland, Quantum versus classical dynamics in the optical centrifuge, *Phys. Rev. A* **96**, 033411 (2017).
- [19] T. Armon and L. Friedland, Quantum versus classical effects in the chirped-drive discrete nonlinear Schrödinger equation, *Phys. Rev. A* **100**, 022106 (2019).
- [20] T. Armon and L. Friedland, Quantum versus classical chirps in a Rydberg atom, *Phys. Rev. A* **102**, 052817 (2020).
- [21] I. Barth, I. Y. Dodin, and N. J. Fisch, Ladder Climbing and Autoresonant Acceleration of Plasma Waves, *Phys. Rev. Lett.* **115**, 075001 (2015).
- [22] Y. Shalibo, Y. Rofo, I. Barth, L. Friedland, R. Bialczack, J. M. Martinis, and N. Katz, Quantum and Classical Chirps in an Anharmonic Oscillator, *Phys. Rev. Lett.* **108**, 037701 (2012).
- [23] J. Lin, T. Lai, D. Chuu, and T.-F. Jiang, Quantum dynamics of a diatomic molecule under chirped laser pulses, *J. Phys. B: At. Mol. Opt. Phys.* **31**, L117 (1998).
- [24] K. Mishima and K. Yamashita, A theoretical study on laser control of a molecular nonadiabatic process by ultrashort chirped laser pulses, *J. Chem. Phys.* **109**, 1801 (1998).
- [25] T. Witte, T. Hornung, L. Windhorn, D. Proch, R. de Vivie-Riedle, M. Motzkus, and K.-L. Kompa, Controlling molecular ground-state dissociation by optimizing vibrational ladder climbing, *J. Chem. Phys.* **118**, 2021 (2003).
- [26] D. Willock, *Molecular Symmetry* (Wiley, New York, 2009).
- [27] P. G. Szalay and R. J. Bartlett, Multi-reference averaged quadratic coupled-cluster method: A size-extensive modification of multi-reference CI, *Chem. Phys. Lett.* **214**, 481 (1993).
- [28] S. Chelkowski and A. Bandrauk, Raman chirped adiabatic passage: A new method for selective excitation of high vibrational states, *J. Raman Spectrosc.* **28**, 459 (1997).
- [29] J. Davis and W. Warren, Selective excitation of high vibrational states using Raman chirped adiabatic passage, *J. Chem. Phys.* **110**, 4229 (1999).
- [30] N. Hansen and A. Ostermeier, Adapting arbitrary normal mutation distributions in evolution strategies: The covariance matrix adaptation, in *Proceedings of the 1996 IEEE International Conference on Evolutionary Computation* (IEEE, Piscataway, NJ, 1996), pp. 312–317.
- [31] H. Sakai, S. Minemoto, H. Nanjo, H. Tanji, and T. Suzuki, Controlling the Orientation of Polar Molecules with Combined Electrostatic and Pulsed, Nonresonant Laser Fields, *Phys. Rev. Lett.* **90**, 083001 (2003).
- [32] K. Oda, M. Hita, S. Minemoto, and H. Sakai, All-Optical Molecular Orientation, *Phys. Rev. Lett.* **104**, 213901 (2010).
- [33] F. Habel and V. Pervak, Dispersive mirror for the mid-infrared spectral range of 9–11.5  $\mu\text{m}$ , *Appl. Opt.* **56**, C71 (2017).
- [34] R. Zhang, J. Teipel, X. Zhang, D. Nau, and H. Giessen, Group velocity dispersion of tapered fibers immersed in different liquids, *Opt. Express* **12**, 1700 (2004).
- [35] K. Ohmori, H. Katsuki, H. Chiba, M. Honda, Y. Hagihara, K. Fujiwara, Y. Sato, and K. Ueda, Real-Time Observation of Phase-Controlled Molecular Wave-Packet Interference, *Phys. Rev. Lett.* **96**, 093002 (2006).
- [36] H. Katsuki, H. Chiba, B. Girard, C. Meier, and K. Ohmori, Visualizing picometric quantum ripples of ultrafast wave-packet interference, *Science* **311**, 1589 (2006).
- [37] K. Ohmori, Y. Sato, E. E. Nikitin, and S. A. Rice, High-Precision Molecular Wave-Packet Interferometry with HgAr Dimers, *Phys. Rev. Lett.* **91**, 243003 (2003).
- [38] B. O. Roos, P. R. Taylor, and P. E. Sigbahn, A complete active space SCF method (CASSCF) using a density matrix formulated super-CI approach, *Chem. Phys.* **48**, 157 (1980).
- [39] T. H. Dunning, Jr., Gaussian basis sets for use in correlated molecular calculations. I. The atoms boron through neon and hydrogen, *J. Chem. Phys.* **90**, 1007 (1989).
- [40] R. A. Kendall, T. H. Dunning, Jr., and R. J. Harrison, Electron affinities of the first-row atoms revisited. Systematic basis sets and wave functions, *J. Chem. Phys.* **96**, 6796 (1992).
- [41] B. P. Prascher, D. E. Woon, K. A. Peterson, T. H. Dunning, and A. K. Wilson, Gaussian basis sets for use in correlated

- molecular calculations. VII. Valence, core-valence, and scalar relativistic basis sets for Li, Be, Na, and Mg, *Theor. Chem. Acc.* **128**, 69 (2011).
- [42] M. W. Schmidt, K. K. Baldridge, J. A. Boatz, S. T. Elbert, M. S. Gordon, J. H. Jensen, S. Koseki, N. Matsunaga, K. A. Nguyen, S. Su *et al.*, General atomic and molecular electronic structure system, *J. Comput. Chem.* **14**, 1347 (1993).
- [43] M. S. Gordon and M. W. Schmidt, Advances in electronic structure theory: GAMESS a decade later, in *Theory and Applications of Computational Chemistry* (Elsevier, Amsterdam, 2005), pp. 1167–1189.
- [44] K.-P. Huber and G. Herzberg, Constants of diatomic molecules, in *Molecular Spectra and Molecular Structure IV*, Vol. 4 (Springer US, Boston, MA, 1979), p. 8–689.
- [45] W. van Dijk and F. M. Toyama, Accurate numerical solutions of the time-dependent Schrödinger equation, *Phys. Rev. E* **75**, 036707 (2007).
- [46] M. Feit, J. Fleck, Jr., and A. Steiger, Solution of the Schrödinger equation by a spectral method, *J. Comput. Phys.* **47**, 412 (1982).
- [47] T. Barthel and Y. Zhang, Optimized Lie-Trotter-Suzuki decompositions for two and three non-commuting terms, *Ann. Phys. (NY)* **418**, 168165 (2020).
- [48] S. Tanimura, K. Yasuoka, and T. Ebisuzaki, Molecular dynamics simulations of the homogeneous nucleation of UF<sub>6</sub> and SF<sub>6</sub> molecules: Effects of the intramolecular vibrational relaxations on the nucleation rates, *J. Chem. Phys.* **109**, 4492 (1998).
- [49] D. Goswami and W. Warren, Control of chemical-dynamics by restricting intramolecular vibrational relaxation, *J. Chem. Phys.* **99**, 4509 (1993).
- [50] D. Goswami, Multiphoton coherent control in complex systems, *J. Opt. B: Quantum Semiclass. Opt.* **7**, S265 (2005).
- [51] M. Sugawara, Suppression of intramolecular vibrational energy redistribution by intense cw-laser fields, *Adv. Phys. Chem.* **2011**, 584082 (2011).
- [52] J. Snoek, H. Larochelle, and R. P. Adams, Practical Bayesian optimization of machine learning algorithms, in *Advances in Neural Information Processing Systems* Vol. 25 (MIT Press, Cambridge, MA, 2012), pp. 2951–2959.
- [53] GPy: A Gaussian process framework in python, <http://github.com/SheffieldML/GPy> (2012).
- [54] N. Lawrence, M. Seeger, and R. Herbrich, Fast sparse Gaussian process methods: The informative vector machine, in *Advances in Neural Information Processing Systems* (MIT Press, Cambridge, MA, 2003), pp. 609–616.
- [55] N. Hansen, The CMA evolution strategy: A tutorial, [arXiv:1604.00772](https://arxiv.org/abs/1604.00772).
- [56] I. Loshchilov, M. Schoenauer, and M. Sebag, Bi-population CMA-ES algorithms with surrogate models and line searches, in *Genetic and Evolutionary Computation Conference (GECCO Companion)* (ACM Press, Amsterdam, Netherlands, 2013) pp. 1177–1184.
- [57] W. Zhu and H. Rabitz, A rapid monotonically convergent iteration algorithm for quantum optimal control over the expectation value of a positive definite operator, *J. Chem. Phys.* **109**, 385 (1998).
- [58] D. B. Foote, Y. Lin, L.-W. Pi, J. M. Ngoko Djiokap, A. F. Starace, and W. T. Hill, Ionization enhancement and suppression by phase-locked ultrafast pulse pairs, *Phys. Rev. A* **96**, 023425 (2017).